The Astrophysical Journal, 758:38 (15pp), 2012 October 10 doi:10.1088/0004-637X/758/1/38

CO_2 ICE TOWARD LOW-LUMINOSITY EMBEDDED PROTOSTARS: EVIDENCE FOR EPISODIC MASS ACCRETION VIA CHEMICAL HISTORY

Hyo Jeong Kim[1], Neal J. Evans II[1], Michael M. Dunham[2], Jeong-Eun Lee[3], and Klaus M. Pontoppidan[4]
[1] Department of Astronomy, The University of Texas at Austin, 2515 Speedway, Stop C1400 Austin, TX 78712-1205, USA; hyojeong@astro.as.utexas.edu
[2] Department of Astronomy, Yale University, P.O. Box 208101, New Haven, CT 06520, USA
[3] Department of Astronomy and Space Science, Kyung Hee University, Yongin-si, Gyeonggi-do 446-701, Republic of Korea
[4] Space Telescope Science Institute, Baltimore, MD 21218, USA
Received 2012 April 9; accepted 2012 August 24; published 2012 September 24

ABSTRACT

We present *Spitzer* IRS spectroscopy of CO_2 ice bending mode spectra at 15.2 μm toward 19 young stellar objects (YSOs) with luminosity lower than 1 $L_\odot$ (3 with luminosity lower than 0.1 $L_\odot$). Ice on dust grain surfaces can encode the history of heating because pure CO_2 ice forms only at elevated temperature, $T > 20$ K, and thus around protostars of higher luminosity. Current internal luminosities of YSOs with $L < 1 L_\odot$ do not provide the conditions needed to produce pure CO_2 ice at radii where typical envelopes begin. The presence of detectable amounts of pure CO_2 ice would signify a higher past luminosity. Many of the spectra require a contribution from a pure, crystalline CO_2 component, traced by the presence of a characteristic band splitting in the 15.2 μm bending mode. About half of the sources (9 out of 19) in the low-luminosity sample have evidence for pure CO_2 ice, and 6 of these have significant double-peaked features, which are very strong evidence of pure CO_2 ice. The presence of the pure CO_2 ice component indicates that the dust temperature, and hence luminosity of the central star/accretion disk system, must have been higher in the past. An episodic accretion scenario, in which mixed CO–CO_2 ice is converted to pure CO_2 ice during each high-luminosity phase, explains the presence of pure CO_2 ice, the total amount of CO_2 ice, and the observed residual $C^{18}O$ gas.

Key words: astrochemistry – ISM: molecules – stars: formation – stars: low-mass – stars: protostars

Online-only material: color figures

1. INTRODUCTION

While the standard star formation model with constant accretion rate (Shu 1977; Shu et al. 1987) predicts that protostars have a luminosity higher than 1.6 $L_\odot$ most of the time, young stellar objects (YSOs) with luminosity lower than 1.6 $L_\odot$ have long been known (Kenyon et al. 1990; Greene et al. 1994; Hartmann & Kenyon 1996). The *Spitzer* Legacy Project, From Molecular Cores to Planet Forming Disks (c2d; Evans et al. 2003) found that 59% of the 112 embedded protostars have luminosity lower than 1.6 $L_\odot$ (Evans et al. 2009). In fact, *Spitzer* found a substantial number of sources with the internal luminosity even below 0.1 $L_\odot$ (Young et al. 2004a; Dunham et al. 2008), which have been called very low luminosity objects (di Francesco et al. 2007). The internal luminosity ($L_{\rm int}$) of an embedded protostar is the luminosity of the central source, excluding luminosity from external heating. Recently, an even lower luminosity protostar ($L_{\rm int} < 0.03 L_\odot$) was discovered as a binary companion to IRAM04191+1522 IRS (Chen et al. 2012). One explanation for such low luminosities is that mass accretion is not a constant process (Kenyon et al. 1990; Enoch et al. 2009b; Dunham et al. 2010b). The low-luminosity sources may be going through a low mass accretion stage between accretion bursts, explaining their currently low luminosities. If mass accretion is episodic, sources with low luminosity may have had much higher accretion rates in the past, and thus had higher luminosity. Imprints of the high-luminosity stage in low-luminosity YSOs would support the idea of episodic mass accretion.

Evidence of past periods of higher luminosity can be found in molecular spectra of the gas and ice phases of low-luminosity sources (Lee 2007; Visser & Bergin 2012). In particular, Pontoppidan et al. (2008) analyzed the general shape of the 15.2 μm CO_2 ice bending mode spectrum toward 50 embedded young stars. The 15.2 μm CO_2 spectrum can be decomposed into multiple components, including a pure CO_2 ice component. The pure CO_2 ice can form by two processes. One is CO_2 segregation out of a CO_2–H_2O mixture. The other is a distillation process, in which CO evaporates from a CO_2–CO mixture, leaving pure CO_2 behind. The former process occurs at a high temperature (50–80 K) and the latter occurs at a lower temperature (20–30 K). Both pure CO_2 formation processes are irreversible (Hagen et al. 1983), since the bond between pure CO_2 ices makes it the most stable phase. Once the pure CO_2 ice has formed, it will not disappear unless it evaporates. Thus, the existence of pure CO_2 ice provides a "chemical memory" of warmer conditions in the past.

The total amount of CO_2 ice, regardless of form, is another indicator of the temperature history. A number of studies of absorption against background stars have shown that CO_2 ice must form in the prestellar phase (Bergin et al. 2005; Knez et al. 2005; Whittet et al. 2009; Chiar et al. 2011). The shape of the 15.2 μm feature toward background stars varies little from cloud to cloud (Whittet et al. 2009), with most (~85 to 90%) of the CO_2 in the CO_2–H_2O mixture and no evidence for a pure CO_2 component, despite variations in the ratio of CO to H_2O ice from cloud to cloud (Whittet et al. 2009). These ices arise from reactions among H, O, and CO on grain surfaces (e.g., Chiar et al. 2011).

Observations of the CO_2 ice feature toward YSOs tend to show higher values of $N(CO_2)$ than the background stars (Pontoppidan et al. 2008), even for background stars with roughly the same extinction (see Figure 5 in Cook et al. 2011). The ratio of CO_2 ice to H_2O ice in spectra toward YSOs is also higher and more variable than toward background stars while

Table 1
The Low-luminosity Sources Observed with *Spitzer* IRS

Source Number[a]	*Spitzer* Source Name	c2d Core Region	R.A. (J2000)	Decl. (J2000)	Internal luminosity[b] ($L_\odot$)	PID
003	SSTc2d J042200.41+153021.2	IRAM04191 + 1522	04:22:00.41	+15:30:21.2	0.08	20604
005	SSTc2d J044112.65+254635.4	TMC1	04:41:12.65	+25:46:35.4	0.36	50295
016	SSTc2d J124539.96−552522.4	DC302.1+7.4	12:45:39.96	−55:25:22.4	0.42	50295
017	SSTc2d J130736.89−770009.7	DC303.8−14.2	13:07:36.89	−77:00:09.7	0.46	50295
021	SSTc2d J165719.63−160923.4	CB68	16:57:19.63	−16:09:23.4	0.54	50295
023	SSTc2d J171122.18−272602.0	B59	17:11:22.18	−27:26:02.0	0.42	50295
024	SSTc2d J181616.39−023237.7	CB130−1	18:16:16.39	−02:32:37.7	0.15	50295
038	SSTc2d J212407.58+495908.9	L1014	21:24:07.58	+49:59:08.9	0.09	20604
043	SSTc2d J222959.52+751403.1	L1251	22:29:59.52	+75:14:03.1	0.21	50295
060	SSTc2d J032637.46+301528.1	Perseus	03:26:37.46	+30:15:28.1	0.69	50295
063	SSTc2d J032738.26+301358.8	Perseus	03:27:38.26	+30:13:58.8	0.20	50295
068	SSTc2d J032845.29+310542.0	Perseus	03:28:45.29	+31:05:42.0	0.26	50295
078	SSTc2d J032923.47+313329.5	Perseus	03:29:23.47	+31:33:29.5	0.20	50295
090	SSTc2d J033229.18+310240.9	Perseus	03:32:29.18	+31:02:40.9	0.20	50295
092	SSTc2d J033314.38+310710.9	Perseus	03:33:14.38	+31:07:10.9	0.14	50295
109	SSTc2d J034421.36+315932.6	Perseus	03:44:21.36	+31:59:32.6	0.11	50295
124	SSTc2d J125342.86−771511.5	Chamaeleon II	12:53:42.86	−77:15:11.5	0.14	50295
161	SSTc2d J160115.55−415235.4	Lupus	16:01:15.55	−41:52:35.4	0.08	50295
182	SSTc2d J162705.23−243629.5	Ophiuchius	16:27:05.23	−24:36:29.5	0.15	50295

Notes.
[a] The source number comes from Dunham et al. (2008).
[b] The source luminosity comes from the relation between 70 μm flux and internal source luminosity (Dunham et al. 2008).

the ratio of CO to H_2O ice is lower for the YSOs, indicative of further processing occurring during the formation of the YSOs (Cook et al. 2011).

The total amount of CO_2 ice formed during the YSO phase depends on the accretion scenario. The episodic accretion scenario gives multiple long periods of low luminosity (Dunham et al. 2010b) instead of the very short period of low luminosity that the continuous accretion model predicts (Shu 1977; Young & Evans 2005). As a result, episodic accretion provides more time for CO to freeze-out and form CO_2 ice. Then, the CO ice can evaporate during episodes of higher accretion and luminosity, leaving the CO_2 ice behind.

The gas phase CO is the final indicator that we consider. Laboratory experiments show that the binding energies of CO and N_2 onto dust grain surfaces are similar (Öberg et al. 2005; Bisschop et al. 2006). After including the updated binding energy, chemo-dynamical models (Lee et al. 2004) predict more CO, as measured by rare isotopes like $C^{18}O$, than is observed (e.g., Chen et al. 2009; Kim et al. 2011). Tying up some of the carbon in CO_2 ice could help to match the observations (Visser & Bergin 2012).

To explain the observed gas phase molecular lines and the total CO_2 ice absorption observed toward one specific low-luminosity source, CB130-1-IRS1, Kim et al. (2011) added some simple ice reactions to an episodic accretion chemical model (Lee et al. 2004; Lee 2007). During low-luminosity periods, the gas phase CO freezes into CO ice, and some CO ice turns into CO_2 ice, creating a CO–CO_2 ice mixture; then, during high-luminosity phases, the CO evaporates, leaving behind CO_2 ice, which evaporates only at a still higher temperature ($T \geqslant 20$ K), depending on the structure of the ice (Pontoppidan et al. 2008). This scenario, developed by Kim et al. (2011) and discussed further by Visser & Bergin (2012), could explain the current low luminosity, the total amount of CO_2 ice, and the strength of the gas phase molecule emission toward CB130-1-IRS1.

In this paper, we test the idea further with higher resolution Infrared Spectrograph (IRS; Houck et al. 2004) spectra for an enlarged source sample and complementary spectroscopy of gas-phase $C^{18}O$ at 1.3 mm. We obtained *Spitzer* IRS, short–high (SH) mode spectroscopy toward 19 YSOs with luminosity lower than 1 $L_\odot$, 4 of them with luminosity lower than 0.1 $L_\odot$. The envelopes around YSOs with luminosity lower than 1 $L_\odot$ have temperatures lower than the CO evaporation temperature. The higher resolution spectra allow decomposition of the 15.2 μm CO_2 ice bending mode spectrum into five different components, including a pure CO_2 component, using the method of Pontoppidan et al. (2008). In Section 2, we explain the sample selection in the current study. We describe the observations in Section 3. In Section 4, we describe the analysis of the *Spitzer* IRS spectrum to get the optical depth and the column density. In Section 5, we present results of the decomposition of ice components. In Section 6, we present the setup and results of the chemical models for different accretion scenarios. In Section 7, we summarize our findings.

2. SOURCES

The sources were selected from the list of low-luminosity objects compiled by Dunham et al. (2008). Table 1 includes the source identification numbers and internal luminosities from that reference, the *Spitzer* source name, the cores or clouds with which a source is associated, *Spitzer* positions, and the Program ID (PID) of the *Spitzer* IRS observation. The internal luminosities are determined by using the correlation between 70 μm flux and the internal luminosity of protostars (Dunham et al. 2008). The sources are Class 0/I objects with luminosities in the range between 0.08 and 0.69 $L_\odot$. We also use sources from Pontoppidan et al. (2008), most of which have luminosities between 1 and 10 $L_\odot$, but some are massive sources with luminosities up to 10^5 $L_\odot$. With the two samples, we can study objects with luminosities from 0.1 $L_\odot$ to 10^5 $L_\odot$.

3. OBSERVATIONS

The *Spitzer* IRS observations of 17 sources were obtained between 2008 November and 2009 May (PID 50295; PI: Michael Dunham) with their background image. Spectra of two more sources, source numbers 003 and 038, were obtained from *Spitzer* archival data, observed in 2005 October and November, respectively (PID 20604; PI: Adwin Boogert). Background images were not observed for these two sources. The observing mode was SH, and the resolving power ($\lambda/\Delta\lambda$) was 600. The data were reduced following the IRS pipeline version S18.7 which produces Basic Calibrated Data (BCD) files. Then we used the bad pixel masks to clean the masked pixels in a set of data. We used the Caltech High-res IRS pipeline (CHIP) to reduce the 17 observed data with background exposure. CHIP is an IDL reduction package for reducing high signal-to-noise SH *Spitzer* IRS spectra (Pontoppidan et al. 2010). CHIP produces better signal-to-noise level but requires the dedicated background exposures. For the two sources without background images, we used SMART (Higdon et al. 2004; Lebouteiller et al. 2010) to do the background subtraction from their own image and to extract spectra from the BCD files. Then we trimmed the end of each order of a spectrum. All 19 sources have clear detections of the CO_2 ice bending mode absorption spectrum. The overlapping regions between orders match well.

The gas-phase molecular line observations were obtained at the CSO[5] in 2010 July. The $C^{18}O$ ($J = 2 \rightarrow 1$) lines were obtained with the fast Fourier transform spectrometer (FFTS) having 8192 channels with a 500 MHz total bandwidth. We used the 230 GHz heterodyne receiver in position switching mode. The main beam efficiency was 0.8, and the velocity resolution was 0.17 km s^{-1}.

4. ANALYSIS

4.1. Reduction of the IRS Spectra

The 15.2 μm CO_2 bending mode spectrum is located between the broad 9.7 μm, and 18–20 μm silicate features, and near the 12 μm H_2O band. To remove the baseline, we constructed a third-order polynomial in the range of 13.3–14.7 μm and 16.2–19.3 μm, and added a Gaussian feature centered at 608 cm^{-1} with FWHM of 73 cm^{-1} for the blue wing of the 18–20 μm silicate feature (Pontoppidan et al. 2008). The 15.2 μm CO_2 bending mode spectra are plotted in Figure 1. The best-fit baselines are given as red dashed lines in the left panels of Figure 1. After the continuum subtraction, we calculated the optical depth of each source by $\tau = -\ln(I/I_0)$, where I_0 is the continuum intensity. Optical depths are plotted in the right panels of Figure 1.

4.2. Decomposition into Ice Components

We used a number of laboratory spectra of CO_2 ices to analyze the 15.2 μm CO_2 bending mode. The available laboratory spectra are CO_2:H_2O mixtures, CO_2:CO mixtures (Ehrenfreund et al. 1997), and pure CO_2 (van Broekhuizen et al. 2006). A minimum of five unique components has been required to fit all previously observed 15.2 μm CO_2 spectra (Pontoppidan et al. 2008). They are a dilute CO_2 (CO_2:CO = 4:100), an H_2O-rich component (CO_2:H_2O = 14:100), a mixture of CO and CO_2 (CO_2:CO = 26:100 and CO_2:CO = 70:100), a pure CO_2 component, and a shoulder component. We did not include the shoulder component, since the shoulder component appears only in massive young stars, but we use both CO_2:CO = 26:100 and CO_2:CO = 70:100 mixtures as separate components. Thus, the number of CO_2 ice components is still five in the current study. We use the laboratory data with the grain shape of the continuous distribution of ellipsoids to convert optical constants to opacities. This is a method to model irregularly shaped grains, successfully used in Pontoppidan et al. (2008). The laboratory ices have been obtained at temperatures between 10 K and 130 K. The laboratory data are not strongly dependent on the temperature. For example, the strength of the pure CO_2 ice component decreases by 1% when the temperature increases from 10 K to 50 K. When temperature increases to 80 K, the strength of the component decreases by 9%. The envelopes of low-luminosity sources have temperatures lower than 20 K. We use the laboratory ices with a temperature at 10 K, except that the pure CO_2 component is at 15 K, for which the laboratory data are available.

The laboratory data for the H_2O-rich CO_2 ice component lie on top of a broad 12 μm H_2O ice feature. We fitted a baseline with a third-order polynomial, and then subtracted the baseline from the laboratory data. The resulting laboratory data used to decompose CO_2 ice features are plotted in Figure 2. The dilute CO_2 component is located at the red part of 15.2 μm bending mode. The CO_2:CO = 70:100 component is located at the blue part of 15.2 μm bending mode. Only the pure CO_2 ice component shows a double-peaked feature.

We varied only the strength of each component to fit the observed optical depth of the CO_2 feature. Then we used a χ^2 minimization technique to obtain the best fit. We have five free parameters, the strengths for each of the five different ice components. The reduced χ^2 of the best fit is listed in Table 2. The best-fit laboratory components are plotted separately and in total in the right panels of Figure 1. In all sources, the water-rich CO_2 ice dominates the shape and the strength of the spectra. The red wing part of the spectrum is determined by the water-rich component. The peak strength is determined by the sum of all the components. The double-peaked features, unique to the pure CO_2 ice, generally agree in wavelength with the laboratory data. We did the component analysis with and without the pure CO_2 ice component included in the fit.

4.3. Column Densities of Ices

To obtain a column density from the optical depth, we integrated the optical depth over wave number, and then divided it by the band strength, A:

$$N(cm^{-2}) = \int \tau(\nu) d\nu / A. \quad (1)$$

We used the band strength from Gerakines et al. (1995). For the pure CO_2 component, the CO_2:CO = 4:100 component, and the CO_2:CO = 26:100 component, $A = 1.1 \times 10^{-17}$ cm molecule^{-1}. For CO_2:CO = 70:100, $A = 0.97 \times 10^{-17}$ cm molecule^{-1}, and the component with CO_2:H_2O = 14:100 has $A = 1.57 \times 10^{-17}$ cm molecule^{-1}. The column densities for each component are listed in Table 2.

4.4. Column Density of Gas Phase CO

The CSO data were reduced with CLASS.[6] The molecular line results are summarized in Table 3. The column density of

[5] This material is based upon work at the Caltech Submillimeter Observatory, which is operated by the California Institute of Technology under cooperative agreement with the National Science Foundation (AST-0838261).

[6] http://www.iram.fr/IRAMFR/GILDAS

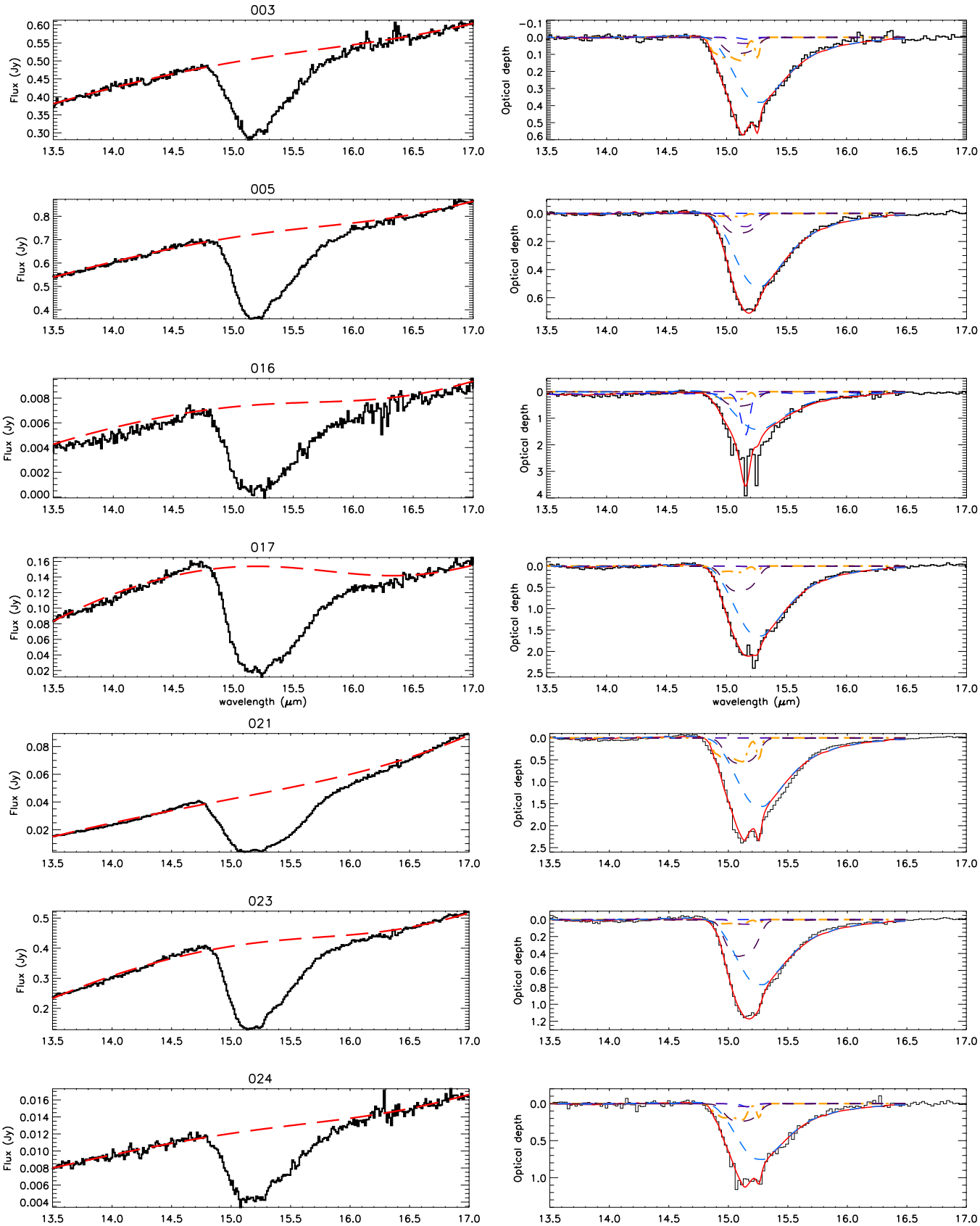

Figure 1. Left panels: observed flux (black solid line) and best-fit continuum (red dashed line). Right panels: optical depth (black solid line), sum of all the ice components (red solid line, best-fit model), pure CO_2 (yellow dash-dot), H_2O-rich CO_2 ice component (blue dashed), and CO–CO_2 mixtures (purple dashed).

(A color version of this figure is available in the online journal.)

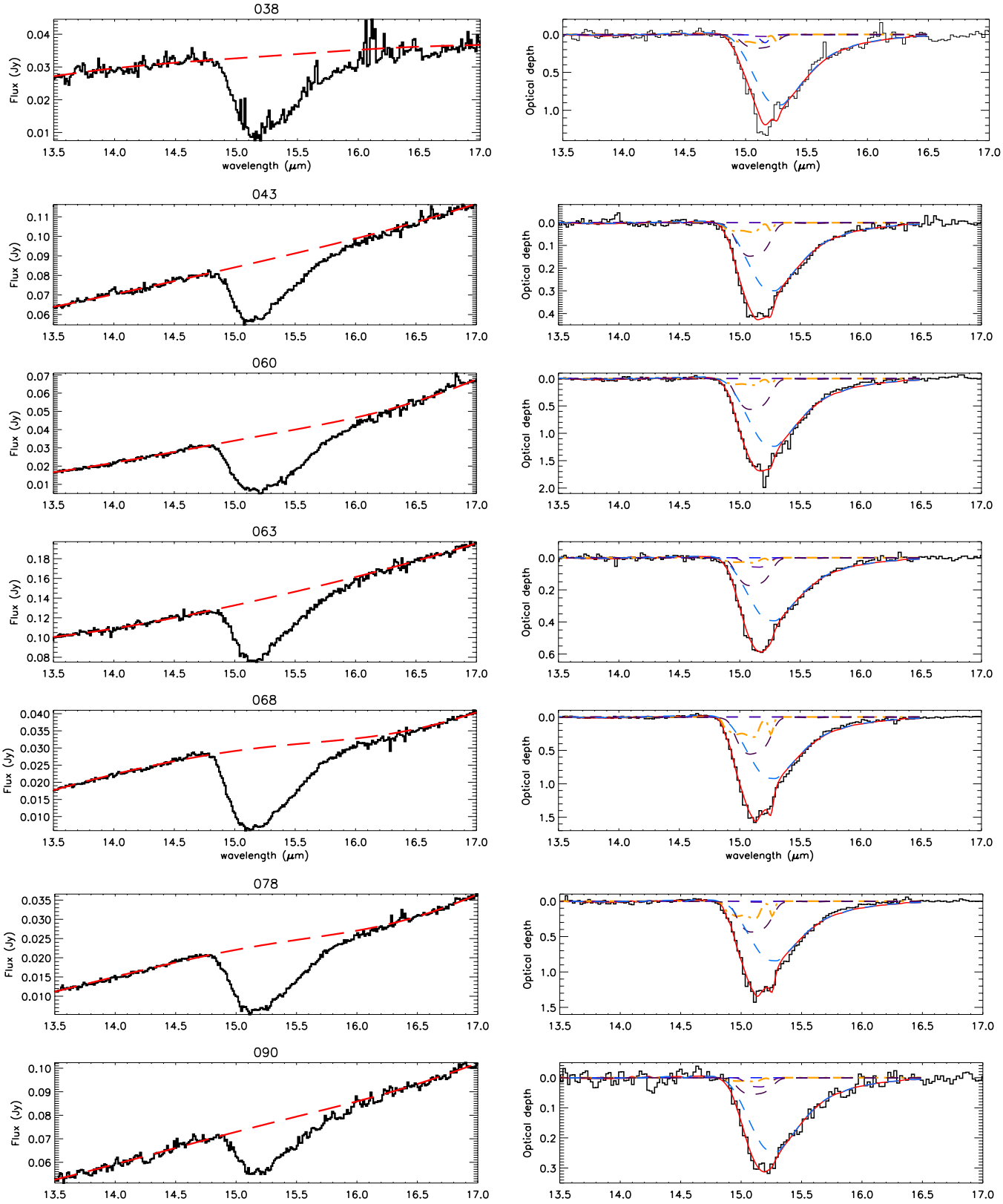

Figure 1. (Continued)

$C^{18}O$ is obtained from

$$N_{C^{18}O} = \frac{3kQ\,exp(E_J/kT_{ex})}{8\pi^3\nu\mu^2 J}\int T_R\,dv, \qquad (2)$$

where $E_J = hBJ(J+1)$, B is the rotational constant; T_{ex} is the excitation temperature; μ is the dipole moment; and Q is the partition function. The parameters B and μ for $C^{18}O$ come from Table 3 of Lee et al. (2003). We assumed $T_{ex} = 10$ K to derive the column density.

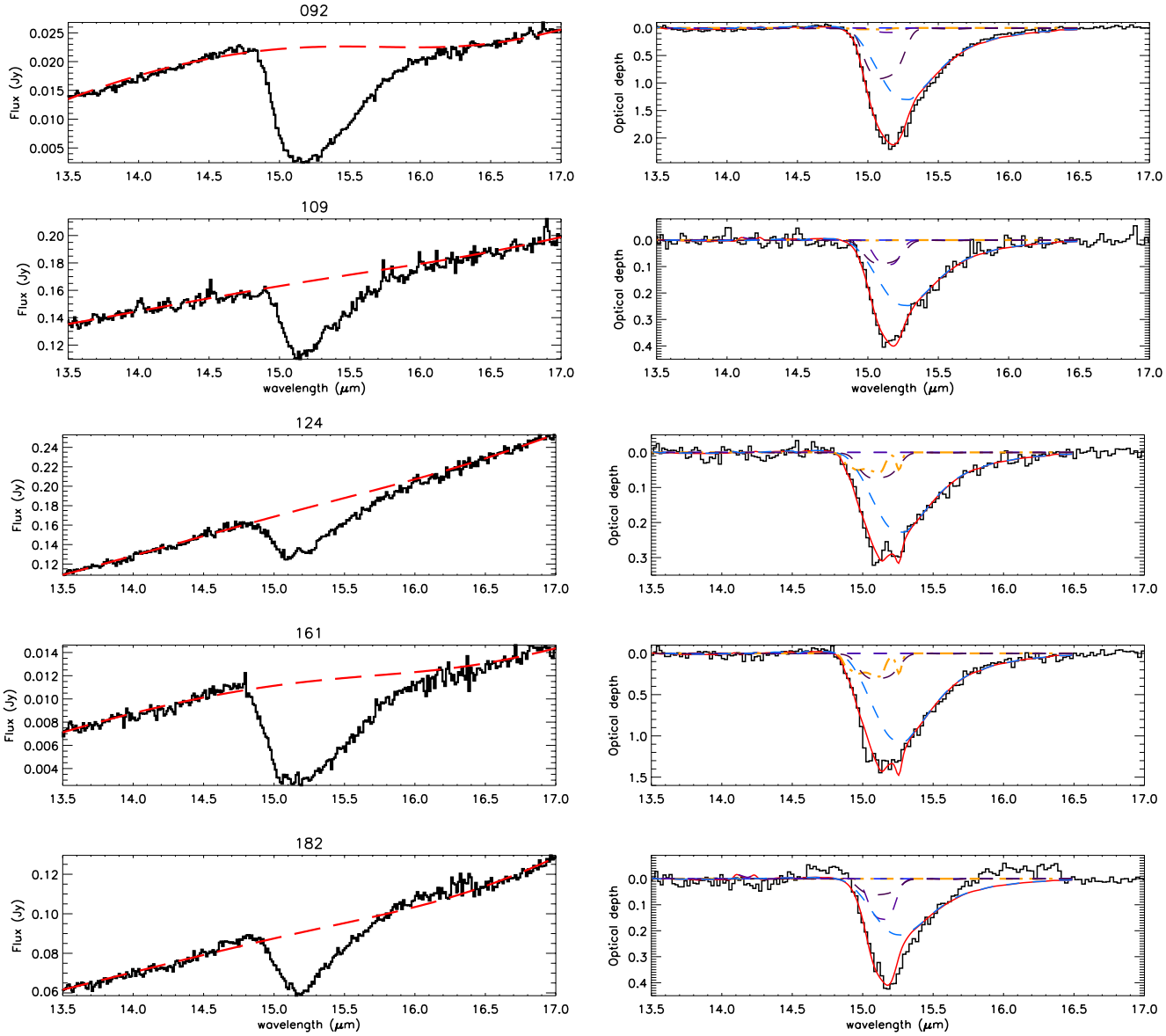

Figure 1. (Continued)

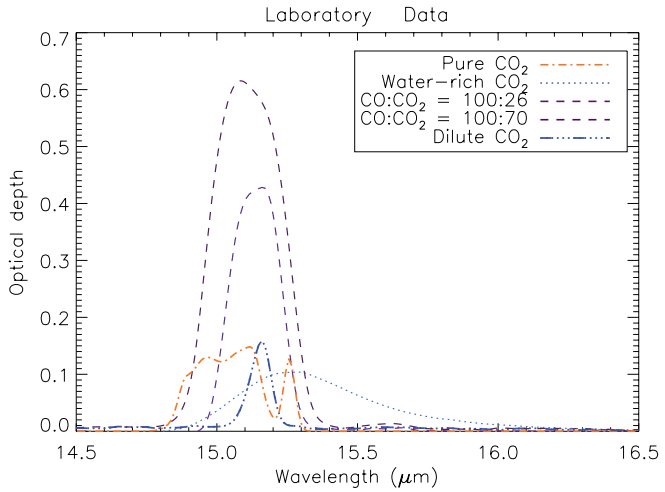

Figure 2. Plot of laboratory data. The yellow line is a pure CO_2 ice, the light blue line is a water-rich CO_2 ice, the blue line is a dilute CO_2 ice, and purple lines are CO:CO_2 ice mixtures. Only the pure CO_2 ice component shows a double peak feature. A baseline is subtracted from a water-rich CO_2 ice component.

(A color version of this figure is available in the online journal.)

5. RESULTS

Double-peaked features are clearly seen for six sources (30%), as indicated in Table 2. As Figure 2 indicates, only the pure CO_2 ice component has a double peak at wavelengths 15.14 μm and 15.26 μm. All the sources with obvious double-peaked features have fits for column density of the pure CO_2 component that are more than 10σ, and the value of χ^2 improved by more than 20% when the pure CO_2 ice component was included. There are three other sources without obvious double-peaked features that satisfy the same criteria for signal to noise and improvement in χ^2, also marked in Table 2. We also consider these to be detections, for a total of 9 detections out of 19 sources (47%). In fact, all but three sources have best-fit values of CO_2 ice column densities with signal-to-noise greater than 10, but we require the improvement in χ^2 because uncertainties in a multi-component fit may be unreliable.

We detected the pure CO_2 ice component with a significant double peak even from the source with $L_{\rm int} = 0.08\,L_\odot$ (Source number: 003). Pontoppidan et al. (2008) found the pure CO_2 ice in 40% of the total 56 sources with clear detections in sources

Table 2
Ice Column Densities of the CO_2 Component

Source Number	Pure CO_2	CO:CO_2 = 100:4	CO:CO_2 = 100:26	CO:CO_2 = 100:70	H_2O:CO_2 = 100:14	Total CO_2	χ^2
003[a]	1.717 ± 0.130	0.063 ± 0.005	0.305 ± 0.023	1.336 ± 0.106	5.949 ± 0.417	9.370 ± 0.680	0.034
005	0.297 ± 0.014	0.000 ± 0.001	0.801 ± 0.031	1.992 ± 0.063	8.108 ± 0.245	11.198 ± 0.353	0.920
016	3.507 ± 0.414	9.235 ± 0.968	0.000 ± 0.002	7.687 ± 0.883	22.288 ± 2.233	42.717 ± 4.500	0.980
017[b]	1.864 ± 0.103	0.086 ± 0.008	0.071 ± 0.005	8.186 ± 0.444	25.543 ± 1.348	35.751 ± 1.908	4.124
021[a]	6.837 ± 0.497	0.000 ± 0.002	0.010 ± 0.012	8.072 ± 0.610	24.355 ± 1.731	39.274 ± 2.853	1.604
023	0.696 ± 0.032	0.000 ± 0.001	0.464 ± 0.019	6.027 ± 0.085	11.985 ± 0.123	19.172 ± 0.260	8.218
024[a]	2.751 ± 0.150	0.256 ± 0.015	0.343 ± 0.026	3.387 ± 0.181	11.762 ± 0.594	18.500 ± 0.966	0.847
038	1.460 ± 0.087	0.623 ± 0.057	0.222 ± 0.011	2.550 ± 0.120	14.490 ± 0.440	19.345 ± 0.715	1.399
043[b]	0.535 ± 0.016	0.000 ± 0.001	0.000 ± 0.001	2.050 ± 0.035	4.673 ± 0.058	7.258 ± 0.109	2.090
060	1.506 ± 0.061	0.000 ± 0.001	0.001 ± 0.010	7.813 ± 0.355	19.302 ± 0.785	28.622 ± 1.212	3.518
063	0.401 ± 0.023	0.000 ± 0.001	0.500 ± 0.023	2.410 ± 0.063	6.124 ± 0.066	9.435 ± 0.175	1.135
068[a]	3.778 ± 0.133	0.000 ± 0.001	0.005 ± 0.009	7.724 ± 0.262	14.364 ± 0.434	25.870 ± 0.838	2.166
078[a]	3.070 ± 0.129	0.000 ± 0.001	0.123 ± 0.073	6.054 ± 0.321	13.141 ± 0.568	22.389 ± 1.091	2.011
090	0.161 ± 0.003	0.000 ± 0.001	0.260 ± 0.024	0.777 ± 0.051	3.842 ± 0.050	5.041 ± 0.128	3.480
092	0.347 ± 0.019	0.000 ± 0.001	0.689 ± 0.123	12.807 ± 0.704	20.304 ± 1.036	34.148 ± 1.882	1.948
109	0.017 ± 0.014	0.000 ± 0.001	0.782 ± 0.048	1.252 ± 0.061	3.860 ± 0.058	5.910 ± 0.182	3.767
124[a]	0.723 ± 0.032	0.000 ± 0.001	0.000 ± 0.001	1.036 ± 0.053	3.548 ± 0.074	5.308 ± 0.159	1.432
161[b]	3.540 ± 0.261	0.000 ± 0.001	0.000 ± 0.001	4.357 ± 0.271	16.695 ± 1.003	24.591 ± 1.536	0.802
182	0.000 ± 0.001	0.000 ± 0.001	1.329 ± 0.033	0.868 ± 0.034	3.378 ± 0.071	5.575 ± 0.139	3.848

Notes. All column densities are in 10^{17} cm^{-2}.
[a] Clearly double-peaked feature.
[b] High signal-to-noise column density of pure CO_2 feature and χ^2 improves by more than 20% when pure CO_2 is included.

Table 3
The $C^{18}O$ ($J = 2 \rightarrow 1$) Observation of Low-luminosity Embedded Sources

Source Number	rms (K)	$\int T_A^* dv$ (K km s^{-1})	v_{LSR} (km s^{-1})	Δv (km s^{-1})	T_A^* (K)	Column Density (cm^{-2})	Reference
003	···	1.68	6.38	0.76	2.06	1.31e+15	(1)
005	0.138	1.31	5.24	0.70	1.77	1.02e+15	
021	0.144	1.25	5.03	0.52	2.29	9.69e+14	
023	0.146	3.13	3.45	1.03	2.86	2.44e+15	
024	0.078	0.48	7.61	0.71	0.64	3.74e+14	(2)
043	0.216	1.20	−4.22	0.82	1.36	9.31e+14	
060	0.140	0.58	5.11	0.52	1.05	4.52e+14	
063	0.135	1.22	5.20	2.59	0.44	9.49e+14	
068	0.141	0.99	8.34	1.41	0.66	7.72e+14	
109	0.138	1.71	8.96	0.84	1.90	1.33e+15	
161	0.172	1.39	4.02	0.77	1.70	1.08e+15	
182	0.199	4.69	4.72	1.20	3.66	3.65e+15	

References. (1) J. H. Chen et al. 2012, in preparation; (2) Kim et al. 2011.

with luminosity higher than 1 $L_\odot$. The current result shows that the presence of pure CO_2 ice is at least as common in low-luminosity protostars as it is in high-luminosity protostars. This is all the more remarkable because absorption in the surrounding molecular cloud from unprocessed CO_2 ice (Whittet et al. 2009) will make the pure CO_2 ice signal harder to see.

CO evaporates from CO_2–CO ice mixture at a temperature 20–30 K. We take the minimum required temperature for pure CO_2 ice formation as 20 K. It is beyond the scope of this paper to explore the parameter space of the structures of the protostellar envelopes, but through model studies, the envelope inner radii of embedded protostars are $\geqslant$100 AU. (Serpens 1: 600 AU, Enoch et al. 2009a; IRAM 04191: 140 AU, Dunham et al. 2006; CB130-1: 350 AU, Kim et al. 2011; L673-7: 140 AU, Dunham et al. 2010a). Many of these individual studies used simple one-dimensional or two-dimensional geometry to approximate the complicated transition between the envelope and disk, and the envelope inner radius is a way of parameterizing this transition with a single value. To match observed SEDs, one must have an inner cutoff to a spherical density profile to avoid having extremely high density material, and thus optical depth. Though 100 AU is not an exact value representing the inner radii of all envelopes, it is a minimum value compared to values found in many models.

Using DUSTY (Ivezic et al. 1999), we calculated a dust temperature around sources with luminosities of 0.7 $L_\odot$ (the highest current luminosity in our sample) and 150 $L_\odot$, more characteristic of the sample of Pontoppidan et al. (2008). For these models, we decreased the inner radius so that we could trace the dust temperature to smaller radii. The dust temperature for the $L_{int} = 0.7\,L_\odot$ protostar (Figure 3) is lower than 20 K everywhere outside about 400 AU. A detailed calculation of the chemistry preceding and during the first hydrostatic core (FHSC) stage confirms this result (Furuya et al. 2012).

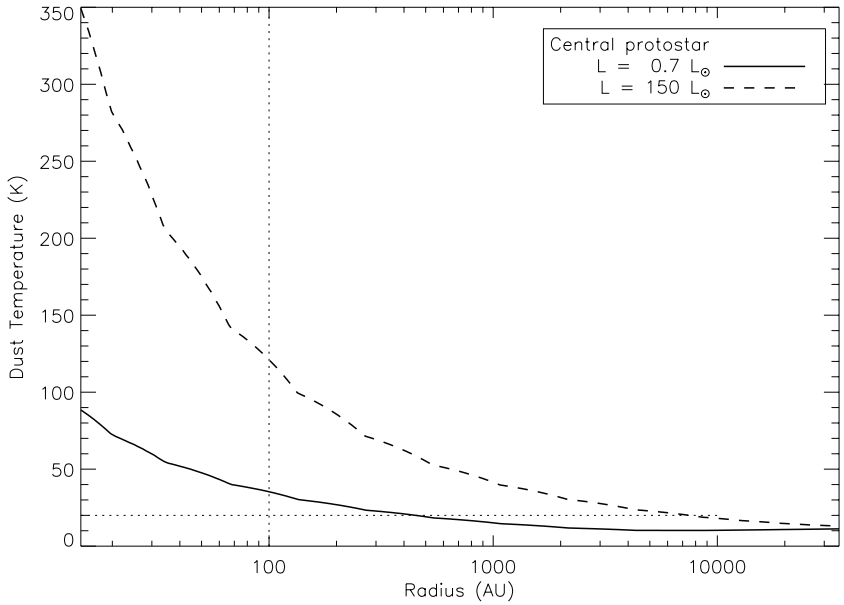

Figure 3. Dust temperatures as a function of radius for two different luminosities, characteristic of the current sample ($L = 0.7\,L_{\odot}$) and the previous sample ($L = 150\,L_{\odot}$). The inner radius in both models is 10 AU, the same as was used in the chemical models used in this paper. The envelope inner radii of embedded protostars are about 100 AU. The horizontal dashed line indicates a dust temperature of 20 K, the minimum required for producing pure CO_2 ice.

In contrast, the model with $150\,L_{\odot}$ has an extended region ($r < 8000$ AU) with dust temperature above 20 K. If the luminosities had always been less than or equal to the current values, pure CO_2 ices should be prominent only in the high-luminosity sample, contrary to our observations.

We can also make a quantitative comparison of the current sample and the sample from Pontoppidan et al. (2008). We plot column densities of each CO_2 ice component versus source luminosities in Figure 4. We divide the sources for convenience into three groups: the current, low-luminosity ($L_{\rm int} < 0.7$) sample; the sources from Pontoppidan et al. (2008) with intermediate luminosity ($0.7 < L_{\rm int} < 100\,L_{\odot}$); and the high-luminosity ($L_{\rm int} > 10^3\,L_{\odot}$) sources. The sources in the current study, with luminosity lower than $0.7\,L_{\odot}$, have a similar pure CO_2 column density range as the intermediate-luminosity sources. For example, the maximum pure CO_2 ice column density detected toward sources with luminosity higher than $1.0\,L_{\odot}$ is 1.06×10^{18} cm^{-2}, while the maximum pure CO_2 ice column density is 6.8×10^{17} cm^{-2} in the source with internal luminosity $0.54\,L_{\odot}$. The amount of pure CO_2 ice does not depend on the current luminosity.

Table 2 and Figure 4 show that the H_2O-rich CO_2 ice component is dominant in all sources. Most of the CO_2 ice exists as a mixture with water regardless of the source luminosity. It takes more energy to segregate CO_2 ice and H_2O ice, so H_2O-rich CO_2 ice is more stable than CO–CO_2 ice mixtures. In the low-luminosity sources, the mixture with CO exhibits more scatter and higher values in some cases than in the high-luminosity sources. The sources with high luminosities may have evaporated much of the CO from CO–CO_2 ice leaving pure CO_2 behind. The total CO_2 ice amount is also low in the high-luminosity sources compared to the spread seen in the low-luminosity sources. The high-luminosity sources could evaporate all the local CO_2 ices, leaving only the ices in the extended cloud. The pure CO_2/total CO_2 ratios have almost the same range of variation in the low- and intermediate-luminosity groups. This result adds to the evidence for higher luminosities in the past for the sources with current low luminosities.

6. DISCUSSION

6.1. Chemical Models with Episodic Accretion

One plausible reason for the presence of the pure CO_2 ice component in low-luminosity young stars is episodic accretion (Kenyon et al. 1990; Vorobyov & Basu 2005). In this model, the material falling in from the envelope is not continuously accreted onto the star. Instead, it piles up on a disk and accretes onto a star in a short-lived burst, when the disk becomes unstable. The burst period can give enough heating to form pure CO_2 ice in the envelope. Once the pure CO_2 ice has formed, it will persist. A series of "freeze-thaw" cycles combined with irreversible chemical processes can make distinct chemical signatures not possible in a model with monotonic temperature behavior.

In addition to the pure CO_2 evidence, the total amount of CO_2 ice, including that in mixed ices, can be explained by long periods of low luminosity between episodic accretion bursts, as predicted in an episodic accretion scenario. The source luminosity steadily increases in a continuous accretion model as the mass of the central star grows. Larger and larger fractions of the envelope become too warm for freeze-out. In contrast, the episodic accretion model has multiple long periods of low luminosity (Dunham et al. 2010b), punctuated by episodes of higher luminosity. More ice can form during the low-luminosity periods.

With chemical evolution modeling, we can relate the amount of observed CO_2 ice to the accretion scenario. We use the evolutionary chemo-dynamical model by Lee et al. (2004) to test this idea. The model calculates the chemical evolution of a core from the prestellar core to the embedded protostellar core stage. At each time step, the density profile, the dust temperature, the gas temperature, and the abundances are calculated self-consistently.

The original chemical models can produce CO_2 ice only by freezing of gas-phase CO_2. We added a second route to CO_2 ice production into the chemical network. Until recently there was no known exact chemical pathway for CO_2 ice formation in cold environments (D'Hendecourt et al. 1985; Roser et al.

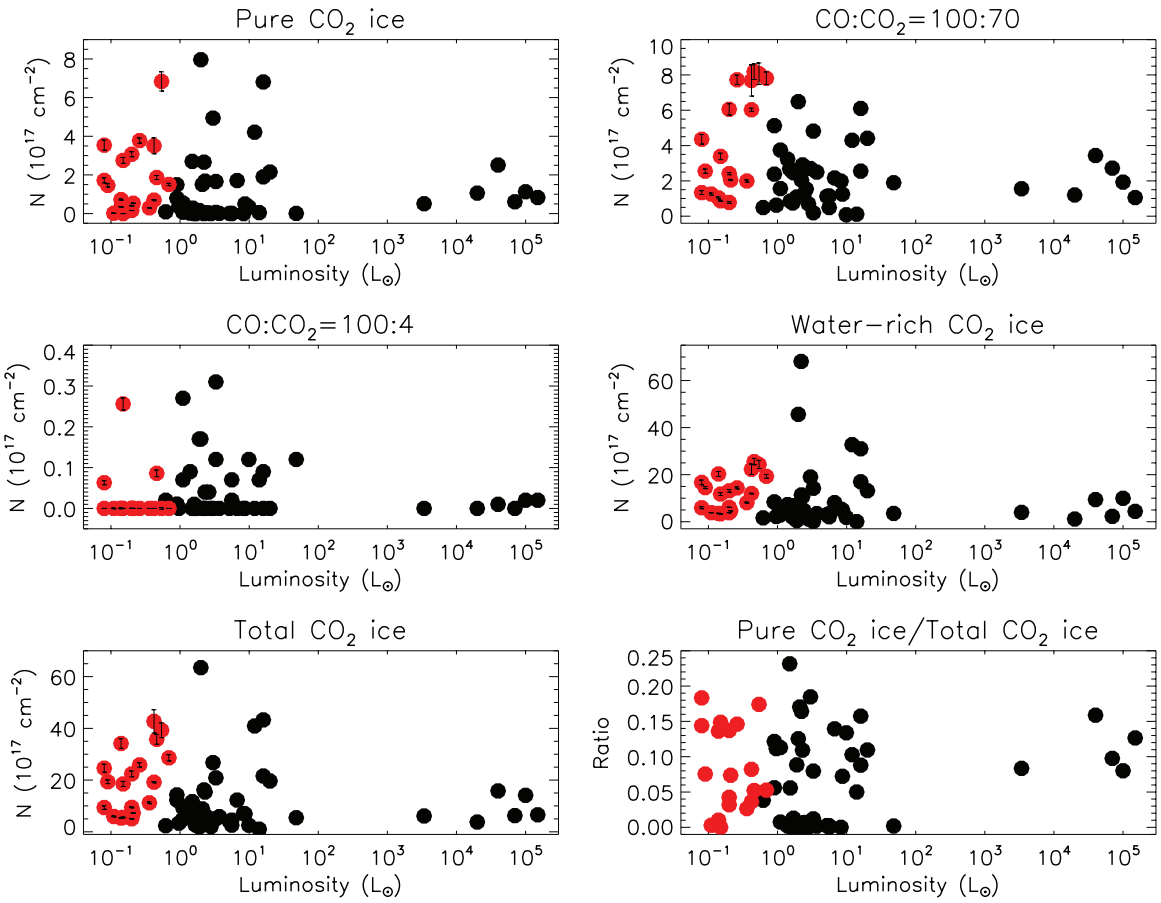

Figure 4. Column densities of the different CO_2 ice components and the total plotted vs. source luminosities. The red points are from the current study; the black points are from Pontoppidan et al. (2008).

(A color version of this figure is available in the online journal.)

2001; Ruffle & Herbst 2001). Recently, Garrod & Pauly (2011) suggested that CO ice turns into CO_2 ice on cold interstellar dust grain surfaces in the presence of OH radicals. Laboratory experiments support this idea (Oba et al. 2010). The process can occur at dust temperatures as low as ∼10–12 K. In our study, we did not include the full reaction of CO and OH radicals because the kinetics of CO_2 ice formation on surfaces is an active field of research with no clear answer so far. Instead we adopted a simple model. When the dust temperature is below the CO ice freezing point, $(100 - x)\%$ of the CO gas turns into CO ice and $x\%$ turns into CO_2 ice.

We ran two kinds of chemical models, those with and those without the additional pathway to CO_2 ice from CO. For each kind of chemical model, we ran two kinds of models for the luminosity evolution, for a total of four kinds of models. The first luminosity model assumes continuous accretion. We adopt the luminosity evolution profile from Young & Evans (2005) including the FHSC stage (Larson 1969; Boss 1993; Masunaga et al. 1998; Furuya et al. 2012). Without the FHSC, the luminosity evolution does not have a stage with luminosity lower than 1.0 $L_\odot$, so we use the model with the FHSC stage. In this picture, the low-luminosity sources would be in the FHSC stage. The second is an episodic accretion model from Dunham et al. (2010b). In this model, the episodic accretion is included in a simple, idealized way. The model assumes no accretion from disk to star most of the time, but steady infall from envelope to disk. When the disk mass reaches 0.2 times the stellar mass, then an accretion burst occurs with luminosity 100 times more than the usual value. We used the model of a 1 $M_\odot$ envelope from Dunham et al. (2010b). The luminosity evolutions of the continuous model and the episodic accretion model are plotted in the top panels of Figures 5 and 6, respectively. At early time steps, up to 20,000 yr, both the continuous accretion model and the episodic accretion model evolve in the same way, going through an FHSC stage. The luminosity increases monotonically until it reaches 0.01 $L_\odot$. After the FHSC stage ends, the accretion luminosity increases rapidly, so there is a luminosity gap between 0.01 $L_\odot$ and 1 $L_\odot$ in the continuous accretion model and a gap between 0.01 $L_\odot$ and 0.1 $L_\odot$ in the episodic accretion model.

At each time step, we calculate the dust temperature with DUSTY (Ivezic et al. 1999), and the gas temperature with a gas energetics code (Doty & Neufeld 1997; Young et al. 2004b) using the same modeling set up as Kim et al. (2011). Then the chemical evolution of 512 gas parcels is calculated as each falls into the central region. We assumed the surface binding energy of species onto bare SiO_2 dust grains. The chemical calculation includes interactions between gas and dust and gas-phase reactions. Then the abundance profile at each time step is calculated. To compare models with ice observations, we calculated the total CO_2 ice column density at each time step. We do not track the different components of the CO_2 ice, as the chemical reactions between them are not well established, so we will compare the results to only the total CO_2 ice.

To compare to the observations of gas phase CO, we use the distributions of density, gas temperature, abundance, and

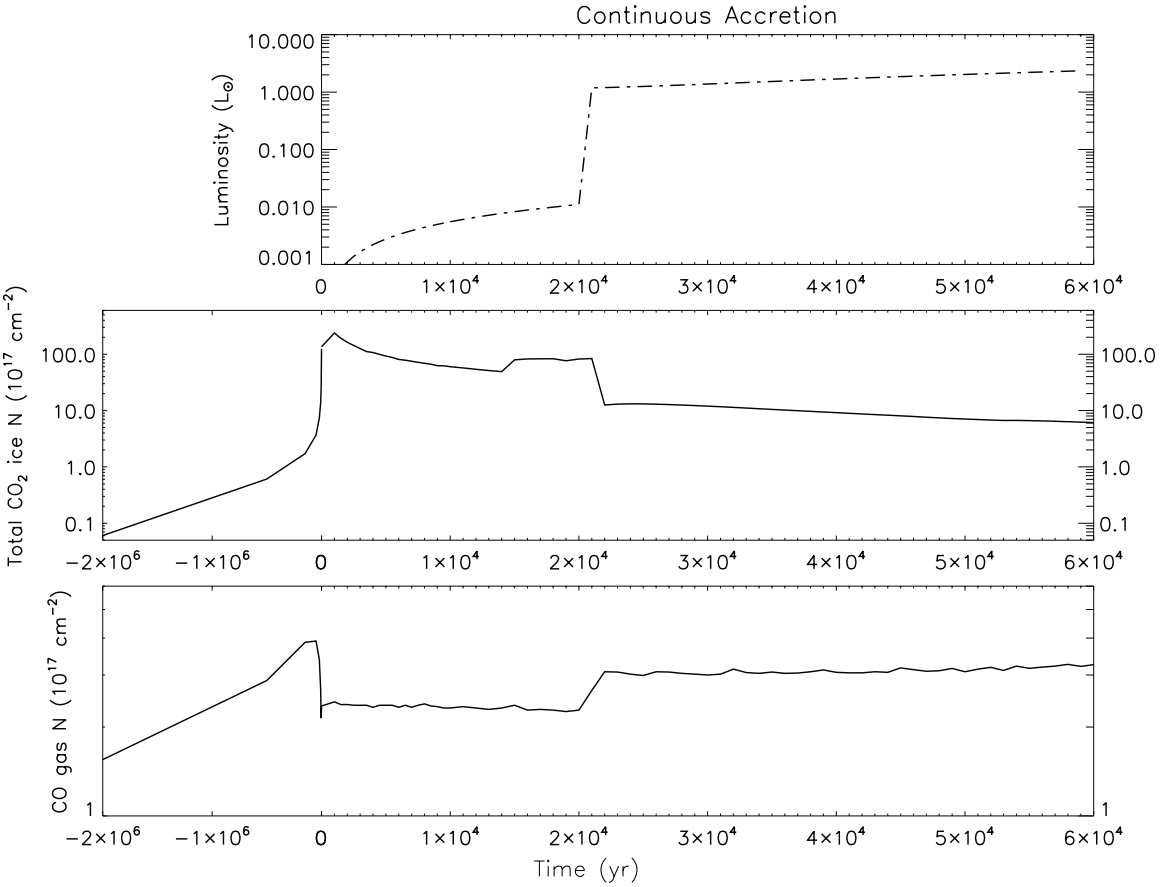

Figure 5. Top panel: the luminosity evolution of the continuous accretion model. Middle panel: the CO_2 ice column density evolution in the constant accretion model with 10% CO ice to CO_2 ice conversion. Bottom panel: the gas phase CO column density evolution in the constant accretion model with 10% CO ice to CO_2 ice conversion. The chemical model includes a long prestellar core stage and an FHSC stage. The time axis is compressed when $t < 0$ since evolution is slow during that time.

velocity at each time step to calculate the distribution of $C^{18}O$ over its energy levels and then simulate the observations by integrating through the envelope and convolving the intensity with a beam matched to the observations. Then we derive the "observed" column density of $C^{18}O$, using the same procedure as used for the observations. The column density of gas phase CO is then obtained by multiplying the $C^{18}O$ column density by the isotope ratio (540; Jørgensen et al. 2004). Because of the limited spatial resolution of the observations and assumptions involved in calculating the observed column density, this "observed" column density from the models will differ from the true column density, but it provides the best comparison to observations.

Models were run with different values of x, the percentage of freezing CO that goes into CO_2 ice. The best match to the observations was found for $x = 10$, so we focus the rest of the discussion on those models. First we discuss the model with a constant accretion rate, followed by that with episodic accretion.

In the model with constant accretion (Figure 5) the luminosity increases monotonically with time once the FHSC forms (top panel). The other two panels in Figure 5 show the total column density in CO_2 ice and in CO gas; they include the prestellar phase ($t < 0$), when the core is assumed to pass through a series of Bonnor–Ebert spheres of increasing central concentration. Since evolution in this phase is slow, the time axis is condensed. During this phase, the "observed" gas-phase CO increases by a factor of about two because the increasing central density increases the excitation of the $C^{18}O$. The CO_2 ice column density increases as gas-phase CO_2 freezes out. These processes accelerate at the later stages of highest central density, but the freeze-out of CO begins to decrease the gas phase column density toward the end of the prestellar evolution. At $t = 0$, the prestellar core evolution is ended by the formation of the FHSC. At $t > 0$, the luminosity of the FHSC grows slowly, and some CO_2 ice evaporates, but it still dominates the gas phase CO column density until the true protostar forms at $t = 2 \times 10^4$ yr. There is a slight increase in the CO_2 ice toward the end of the FHSC phase owing to the conversion of CO ice to CO_2 ice. After $t = 2 \times 10^4$ yr, the luminosity increases as the stellar mass grows ($L \propto M$) and the CO_2 gradually declines while the gas phase CO increases. However, the CO_2 ice column density is still about twice the gas-phase CO column density.

Figure 6 shows the same graphs for the model of episodic accretion. The evolution through the FHSC phase is identical to that of the constant accretion model, but the differences begin with the first episode of enhanced accretion. The dramatic increase in luminosity causes a sharp increase in the gas phase CO, at the expense of the CO_2 ice. After the accretion burst ends, the CO begins to freeze again and the CO_2 ice builds up. This cycle is repeated, with the balance of the C shifting between ice and gas through each accretion cycle, but more ice forms in later quiescent cycles because there is more time between bursts and the luminosity between bursts is slightly lower as the steady state accretion rate is lower. Also, some CO_2 ice persists in the cooler parts of the envelope in each cycle. After the last accretion burst, the luminosity declines slowly and the CO_2 ice

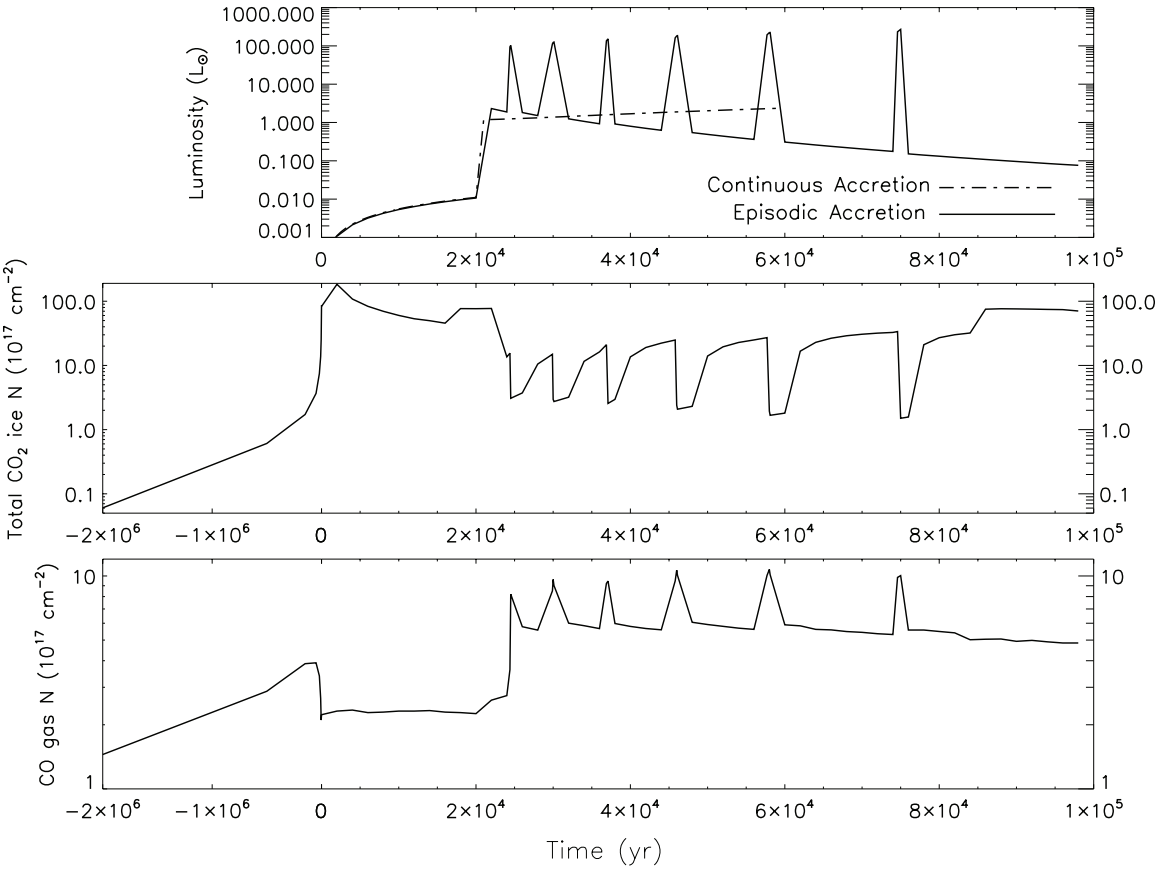

Figure 6. Top panel: the luminosity evolution of the episodic accretion model. The dash-dot line is the luminosity of the continuous accretion model for comparison. Second panel: the total CO_2 ice column density evolution in the episodic accretion model with 10% CO ice to CO_2 ice conversion. Third panel: the gas phase CO column density evolution in the chemical model including the episodic accretion model with 10% CO ice to CO_2 ice conversion.

increases at the expense of the gas phase CO, but this process is limited by processes that continually evaporate some CO. The evolution of the ice and gas components is similar to that shown in Visser & Bergin (2012); differences can mostly be attributed to the fact that our model follows the gas as it falls in, unlike the single-point models in Visser & Bergin (2012).

6.2. Comparison to Observations of Total CO_2 Ice

In Figure 7, we compare the model results and the observational data. The green dots are the observed total CO_2 ice column density from both the current study and Pontoppidan et al. (2008). The observed source luminosities range from 0.1 $L_\odot$ to 90 $L_\odot$. The continuous model does not have luminosities higher than 2.4 $L_\odot$, and the simple, bimodal, episodic accretion model does not cover the luminosity range between 2.6 $L_\odot$ and 90 $L_\odot$. Therefore, we compare the model and observations only between 0.1 $L_\odot$ and 2.5 $L_\odot$.

Both the original episodic accretion model and the continuous accretion model, with the only path to CO_2 ice being freeze-out of CO_2 gas, underestimate the observed column densities by an order of magnitude. The detailed model of FHSC formation and evolution (Furuya et al. 2012) confirms this result. Matching the observations requires the extra pathway in which CO ice is converted to CO_2 ice. Of the two models with this pathway, the continuous model predicts only a small range of CO_2 ice column densities. The episodic accretion model with conversion of CO ice to CO_2 ice describes both the luminosity spread and the spread in observed total CO_2 column density reasonably well.

The total column density of CO_2 ice at the end of the prestellar core evolution is about 1×10^{18} cm^{-2}, which is similar to column densities seen toward background stars (e.g., Whittet et al. 2009). Consequently, the accumulation of CO_2 ice in the quiescent cloud before the formation of the core would roughly double the column density in our models, which do not explicitly include this evolution. Differences from cloud to cloud and from YSO to YSO in the amount of this absorption from the quiescent cloud could explain some of the scatter, allowing the continuous accretion model to fit the data better. However, much of the scatter lies in the regime of $N(CO_2)$ above the values usually seen toward background stars (Whittet et al. 2009).

6.3. Comparison to Observations of $C^{18}O$ Gas

Another check on the models is provided by the residual amount of $C^{18}O$ gas. Leaving out the two sources with the highest CO column density, the average $C^{18}O$ gas column density is 9.18×10^{14} cm^{-2}. We round off to $\sim 10^{15}$ cm^{-2} as a residual $C^{18}O$ gas column density, which is plotted as a horizontal line in Figure 8. The four models are plotted in four different panels for comparison to the data. After a certain amount of time, the $C^{18}O$ gas predicted by the constant accretion models converges to a roughly constant value, $N \sim 6 \times 10^{14}$ cm^{-2}, lower than the mean value. In the episodic accretion model, $C^{18}O$ gas evaporates after each episodic accretion burst, but $N \sim 10^{15}$ cm^{-2} most of the time, as observed. Of course, $C^{18}O$ emission can also come from the larger cloud. An example may be source 182, with the largest $C^{18}O$ column density; this source is in the Ophiuchus cloud,

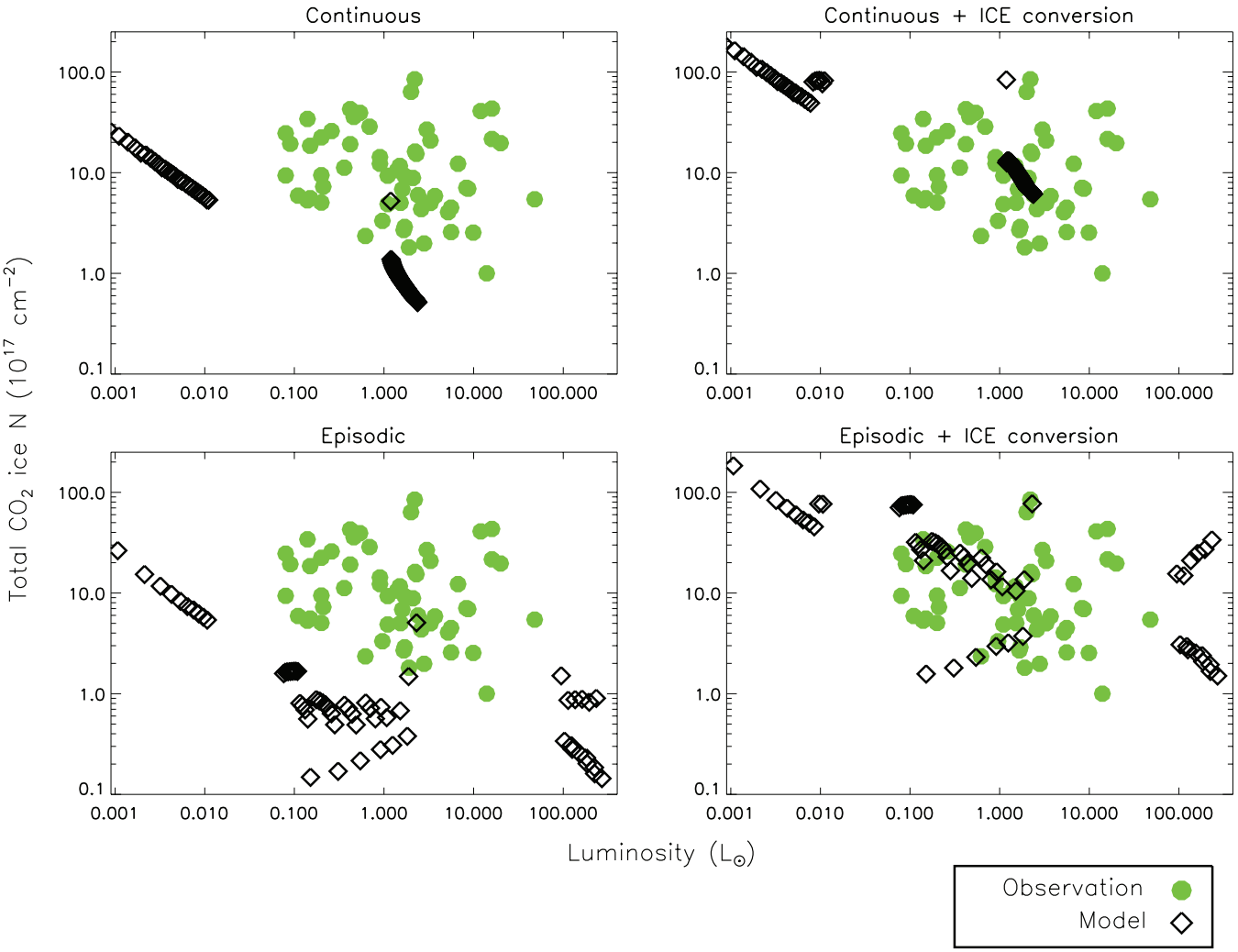

Figure 7. Column densities of CO_2 ice (total) from observations and each of the four luminosity-chemical model combinations. The upper panels have continuous accretion while the lower panels have episodic accretion. The left panels have standard chemical models while the right panels include the extra pathway for CO_2 ice formation. The observed column densities are plotted as green dots, while the model predictions are plotted as black diamonds.

(A color version of this figure is available in the online journal.)

which has large column densities even along lines of sight that do not intercept YSOs.

The different predictions arise from the different abundance profiles. The abundance profiles at time step 60,000 yr, the last time step in the continuous accretion model, are plotted in Figure 9, along with those from the episodic accretion models, which are in a high-luminosity state at this time. The high luminosity has heated the envelope, and thus raised the gas phase CO abundance out to much larger radii, compared to the continuous accretion model.

The column density versus luminosity graphs (Figure 10) compare the models to observations. Seven sources are scattered around the predictions of the model with episodic accretion and CO to CO_2 ice conversion. Two sources lie well above and two lie well below the predictions. The source with the least amount of $C^{18}O$ gas is CB130-1. That source was best fit with a model in which 80% of the CO ice turns into CO_2 ice (Kim et al. 2011), which is much higher than used here. Most source are better matched if 10% of CO ice turns to CO_2 ice.

The current models provide a proof of concept for episodic accretion models to explain the observed CO_2 ice and gas-phase CO abundances, but they can be improved by future work. The episodic accretion included in this study is a simple and idealized model with extreme luminosity variations and does not include the absorption from the larger cloud. It does not cover the luminosity range between 2.3 $L_\odot$ and 90 $L_\odot$. Figure 7 shows that there is a luminosity gap between 2.3 $L_\odot$ and 90 $L_\odot$ in the episodic accretion scenario, while the observed sources do have luminosities in the range between 3 $L_\odot$ and 100 $L_\odot$. Using more realistic models of the accretion history and a range of envelope masses (Offner & McKee 2011; Dunham & Vorobyov 2012) will allow more detailed comparison to the observations.

6.4. Is Episodic Accretion a Unique Explanation?

In this paper, we have shown that a scenario of episodic accretion as modeled by Dunham et al. (2010b) can explain the presence of a component of pure CO_2 ice in the observed 15.2 μm absorption feature, the total column density of all CO_2 ice, and the column density of gas-phase $C^{18}O$ in a sample of low-luminosity protostars. Coupled with the ability of such a scenario to also explain the observed protostellar luminosity distribution (Vorobyov & Basu 2009; Dunham et al. 2010b; Dunham & Vorobyov 2012) and with the existence of other,

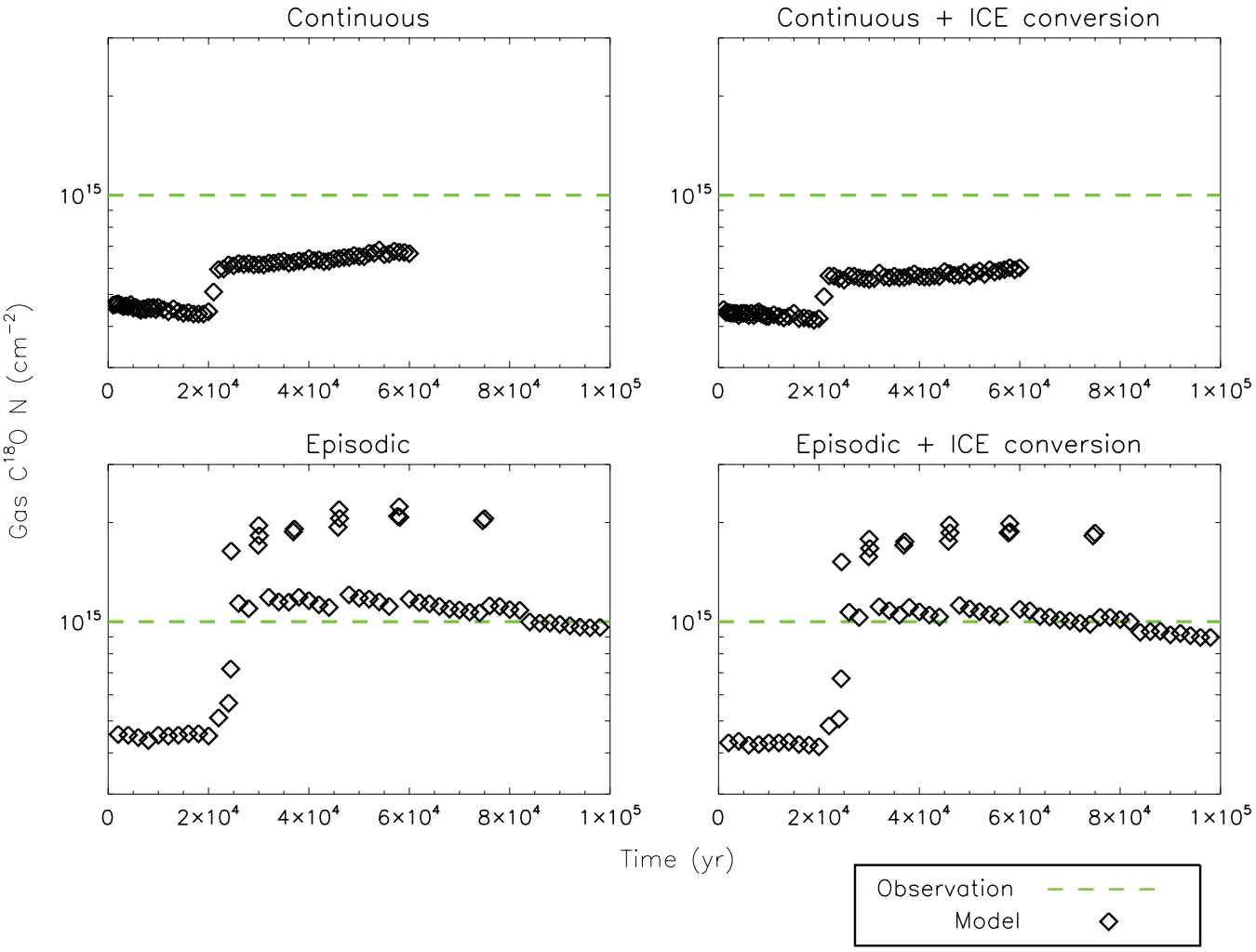

Figure 8. Gaseous $C^{18}O$ column density from each of the four luminosity-chemical models is plotted vs. time. The upper panels have continuous accretion while the lower panels have episodic accretion. The left panels have standard chemical models while the right panels include the extra pathway for CO_2 ice formation. The dashed line is the typical observed column density of $C^{18}O$ gas.

(A color version of this figure is available in the online journal.)

indirect observational evidence for variable accretion (Dunham & Vorobyov 2012 and references therein), there seems to be strong evidence in favor of the existence of episodic accretion.

However, models predicting other mass accretion and luminosity histories have also been proposed. As first noted by Kenyon et al. (1990), a model in which accretion rates peak early and then decline through the remainder of the protostellar phase could potentially match the observed protostellar luminosity distribution. Models of this type have been advanced by a number of authors (e.g., André et al. 1999; Offner & McKee 2011; Hansen et al. 2012). Dunham & Vorobyov (2012) recently argued that such a scenario by itself is insufficient to match observed protostellar luminosities, although their conclusions were based only on the specific set of models considered in their study. A model with an initial peak in the luminosity followed by a long period of decline might reproduce the observations if the initial peak were high enough to produce sufficient pure CO_2 ice and the time spent at lower luminosities were long enough to convert sufficient CO ice to CO_2 ice. Full chemical modeling of such an accretion scenario is required to fully evaluate how well it could reproduce our observations, but this is beyond the scope of our present study. While we acknowledge that such a scenario could possibly explain our ice and gas-phase observations, we consider it somewhat unlikely given the existence of sources like IRAM04191+1522 (source 003) that clearly show double-peaked features indicative of pure CO_2 ice. These are still deeply embedded, Class 0 sources, too young to have already spent sufficient time in the low-luminosity, declining accretion phase in typical models of this type (e.g., André et al. 1999).

Other accretion scenarios may also explain observed protostellar luminosities. Offner & McKee (2011) presented analytic derivations of the protostellar luminosity distribution for different models and concluded that models that tend toward a constant accretion time rather than constant accretion rate produce a greater spread in luminosities and are in better agreement with observations. Hansen et al. (2012) presented simulations including protostellar feedback, both protostellar radiation and outflows, and argued that such simulations can match the means, medians, and standard deviations of the observed protostellar luminosity distribution without episodic accretion. However, they did not compare the full observed and modeled luminosity distributions. The accretion rates in Hansen et al. (2012) and a subset of the models in Offner & McKee (2011), the subset they called the "tapered" models, feature an early peak, followed by a slow decline in the accretion rate throughout the remainder of the embedded phase. As discussed above, such models could

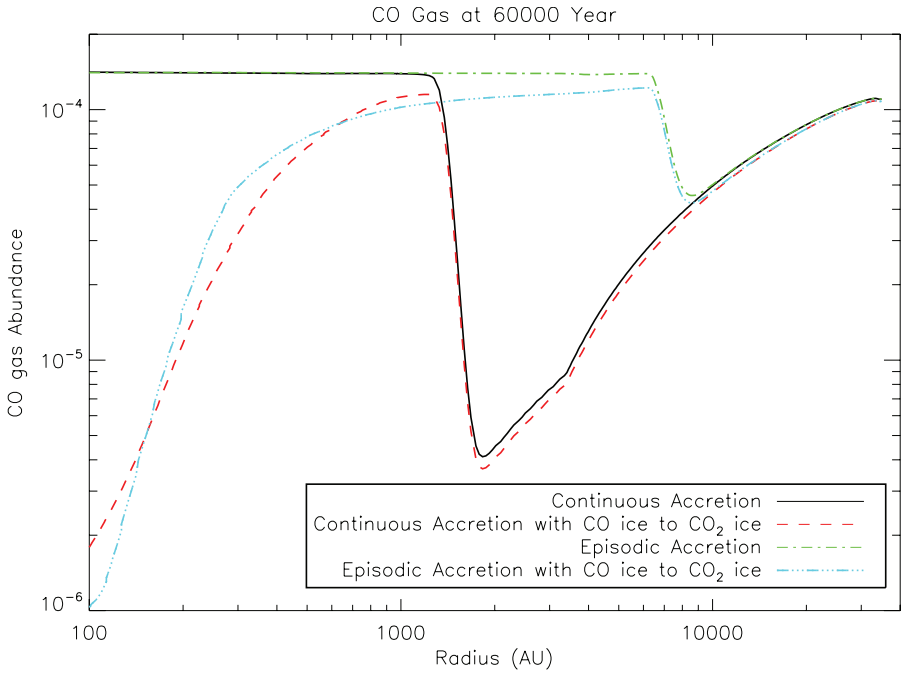

Figure 9. Gaseous CO abundance profile at 60,000 yr from each of the four luminosity-chemical models. The time step is the last time step of the continuous accretion model. At this time, the episodic accretion model is in a high-luminosity state, and the region of high gas phase CO abundance extends to much larger radii than in the continuous accretion model. However, the gas phase CO is still depleted in the inner regions due to conversion into CO_2 ice.

(A color version of this figure is available in the online journal.)

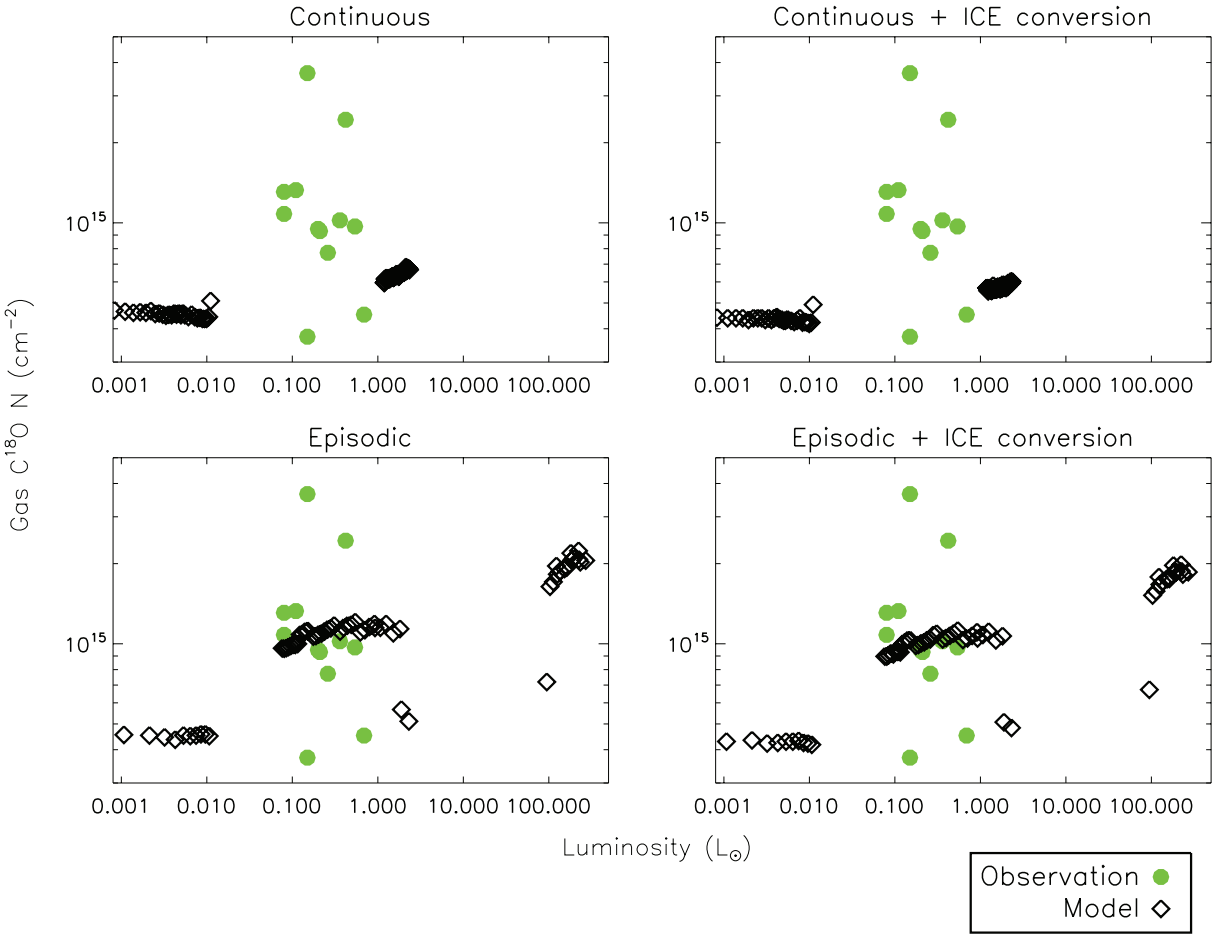

Figure 10. Column densities of $C^{18}O$ gas from observations and each of the four luminosity-chemical model combinations. The upper panels have continuous accretion while the lower panels have episodic accretion. The left panels have standard chemical models while the right panels include the extra pathway for CO_2 ice formation. The observed column densities are plotted as green dots, while the model predictions are plotted as black diamonds.

(A color version of this figure is available in the online journal.)

possibly reproduce our observations, although such models will also be challenged to predict the existence of very young, deeply embedded, very low luminosity protostars with significant pure CO_2 ice.

Detailed calculations of the chemistry for specific evolutionary histories will be needed to test these other models. One possible problem with models that feature one period of high luminosity followed by a long period of low luminosity is that CO ice will form over the pure CO_2 ice, rendering it less visible.

Ultimately, our results do not prove that episodic accretion occurs. They do, however, demonstrate that the past accretion rates must have been higher than the current rates for about half of our targets, and they do show that a scenario of episodic accretion is fully consistent with our observations.

7. CONCLUSION

We detected the pure CO_2 ice double-peaked feature from 6 out of 19 low-luminosity sources with $L \leqslant 1\,L_{\odot}$. Fits to the absorption profile provide strong evidence for pure CO_2 ice in three more sources, for a total of nine (47%). The minimum required temperature to form pure CO_2 ice is 20 K, which is not found in any substantial part of the envelope at the current luminosities of these sources. Detection of pure CO_2 ice strongly indicates higher luminosities in the past. During the time of higher luminosity, the pure CO_2 ice forms and persists into the current low-luminosity stage. The existence of pure CO_2 ice toward such low-luminosity sources is very strong evidence of a phase of higher luminosity in the past, consistent with models of episodic accretion. It also presents a challenge to any alternative model for explaining the luminosity spread seen toward YSOs.

In addition to the luminosity spread of sources (Dunham et al. 2010b; Dunham & Vorobyov 2012), the total CO_2 ice amount and the residual gas phase CO are best explained by episodic accretion with conversion of CO to CO_2 ice. If 10% of CO goes into CO_2 ice when the gas phase CO freezes, observations of most sources are reasonably well matched. There is a substantial spread of values of both total CO_2 ice and gas phase $C^{18}O$ in the observations, which can be explained in an episodic chemistry. However, variations in the ice formation in the larger cloud can also contribute to this scatter. Determinations of other ice components and extinction in the surrounding cloud can help to distinguish these effects.

This material is based upon work supported by the National Aeronautics and Space Administration under RSA 137730 issued by the Jet Propulsion Laboratory. Jeong-Eun Lee was supported by Basic Science Research Program through the National Research Foundation of Korea (NRF) funded by the Ministry of Education, Science and Technology (No. 2012-0002330). Hyo Jeong Kim and Neal J. Evans acknowledge support from NSF grant AST-0607793.

REFERENCES

André, P., Motte, F., & Bacmann, A. 1999, ApJ, 513, L57
Bergin, E. A., Melnick, G. J., Gerakines, P. A., Neufeld, D. A., & Whittet, D. C. B. 2005, ApJ, 627, L33
Bisschop, S. E., Fraser, H. J., Öberg, K. I., van Dishoeck, E. F., & Schlemmer, S. 2006, A&A, 449, 1297
Boss, A. P. 1993, ApJ, 410, 157
Chen, J.-H., Evans, N. J., Lee, J.-E., & Bourke, T. L. 2009, ApJ, 705, 1160
Chen, X., Arce, H. G., Dunham, M. M., & Zhang, Q. 2012, ApJ, 747, L43
Chiar, J. E., Pendleton, Y. J., Allamandola, L. J., et al. 2011, ApJ, 731, 9
Cook, A. M., Whittet, D. C. B., Shenoy, S. S., et al. 2011, ApJ, 730, 124
D'Hendecourt, L. B., Allamandola, L. J., & Greenberg, J. M. 1985, A&A, 152, 130
di Francesco, J., Evans, N. J., II, Caselli, P., et al. 2007, in Protostars and Planets V, ed. B. Reipurth, D. Jewitt, & K. Keil (Tucson, AZ: Univ. Arizona Press), 17
Doty, S. D., & Neufeld, D. A. 1997, ApJ, 489, 122
Dunham, M. M., Crapsi, A., Evans, N. J., II, et al. 2008, ApJS, 179, 249
Dunham, M. M., Evans, N. J., Bourke, T. L., et al. 2010a, ApJ, 721, 995
Dunham, M. M., Evans, N. J., II, Bourke, T. L., et al. 2006, ApJ, 651, 945
Dunham, M. M., Evans, N. J., Terebey, S., Dullemond, C. P., & Young, C. H. 2010b, ApJ, 710, 470
Dunham, M. M., & Vorobyov, E. I. 2012, ApJ, 747, 52
Ehrenfreund, P., Boogert, A. C. A., Gerakines, P. A., Tielens, A. G. G. M., & van Dishoeck, E. F. 1997, A&A, 328, 649
Enoch, M. L., Corder, S., Dunham, M. M., & Duchêne, G. 2009a, ApJ, 707, 103
Enoch, M. L., Evans, N. J., Sargent, A. I., & Glenn, J. 2009b, ApJ, 692, 973
Evans, N. J., Dunham, M. M., Jørgensen, J. K., et al. 2009, ApJS, 181, 321
Evans, N. J., II, Allen, L. E., Blake, G. A., et al. 2003, PASP, 115, 965
Furuya, K., Aikawa, Y., Tomida, K., et al. 2012, arXiv:1207.6693
Garrod, R. T., & Pauly, T. 2011, ApJ, 735, 15
Gerakines, P. A., Schutte, W. A., Greenberg, J. M., & van Dishoeck, E. F. 1995, A&A, 296, 810
Greene, T. P., Wilking, B. A., Andre, P., Young, E. T., & Lada, C. J. 1994, ApJ, 434, 614
Hagen, W., Tielens, A. G. G. M., & Greenberg, J. M. 1983, A&AS, 51, 389
Hansen, C. E., Klein, R. I., McKee, C. F., & Fisher, R. T. 2012, ApJ, 747, 22
Hartmann, L., & Kenyon, S. J. 1996, ARA&A, 34, 207
Higdon, S. J. U., Devost, D., Higdon, J. L., et al. 2004, PASP, 116, 975
Houck, J. R., Roellig, T. L., van Cleve, J., et al. 2004, ApJS, 154, 18
Ivezic, Z., Nenkova, M., & Elitzur, M. 1999, arXiv:astro-ph/9910475
Jørgensen, J. K., Schöier, F. L., & van Dishoeck, E. F. 2004, A&A, 416, 603
Kenyon, S. J., Hartmann, L. W., Strom, K. M., & Strom, S. E. 1990, AJ, 99, 869
Kim, H. J., Evans, N. J., II, Dunham, M. M., et al. 2011, ApJ, 729, 84
Knez, C., Boogert, A. C. A., Pontoppidan, K. M., et al. 2005, ApJ, 635, L145
Larson, R. B. 1969, MNRAS, 145, 271
Lebouteiller, V., Bernard-Salas, J., Sloan, G. C., & Barry, D. J. 2010, PASP, 122, 231
Lee, J.-E. 2007, J. Korean Astron. Soc., 40, 83
Lee, J.-E., Bergin, E. A., & Evans, N. J., II. 2004, ApJ, 617, 360
Lee, J.-E., Evans, N. J., II, Shirley, Y. L., & Tatematsu, K. 2003, ApJ, 583, 789
Masunaga, H., Miyama, S. M., & Inutsuka, S. 1998, ApJ, 495, 346
Oba, Y., Watanabe, N., Kouchi, A., Hama, T., & Pirronello, V. 2010, ApJ, 712, L174
Öberg, K. I., van Broekhuizen, F., Fraser, H. J., et al. 2005, ApJ, 621, L33
Offner, S. S. R., & McKee, C. F. 2011, ApJ, 736, 53
Pontoppidan, K. M., Boogert, A. C. A., Fraser, H. J., et al. 2008, ApJ, 678, 1005
Pontoppidan, K. M., Salyk, C., Blake, G. A., et al. 2010, ApJ, 720, 887
Roser, J. E., Vidali, G., Manicò, G., & Pirronello, V. 2001, ApJ, 555, L61
Ruffle, D. P., & Herbst, E. 2001, MNRAS, 324, 1054
Shu, F. H. 1977, ApJ, 214, 488
Shu, F. H., Adams, F. C., & Lizano, S. 1987, ARA&A, 25, 23
van Broekhuizen, F. A., Groot, I. M. N., Fraser, H. J., van Dishoeck, E. F., & Schlemmer, S. 2006, A&A, 451, 723
Visser, R., & Bergin, E. A. 2012, ApJ, 754, L18
Vorobyov, E. I., & Basu, S. 2005, ApJ, 633, L137
Vorobyov, E. I., & Basu, S. 2009, ApJ, 703, 922
Whittet, D. C. B., Cook, A. M., Chiar, J. E., et al. 2009, ApJ, 695, 94
Young, C. H., & Evans, N. J., II 2005, ApJ, 627, 293
Young, C. H., Jørgensen, J. K., Shirley, Y. L., et al. 2004a, ApJS, 154, 396
Young, K. E., Lee, J., Evans, N. J., II, Goldsmith, P. F., & Doty, S. D. 2004b, ApJ, 614, 252